Optics & Laser Technology 201 (2026) 115253

Contents lists available at ScienceDirect

Optics and Laser Technology

journal homepage: www.elsevier.com/locate/optlastec

Full length article

Laser-Induced periodic surface structures on stainless steel for friction reduction at Sub-Zero temperatures

Armands Leitans [a], Ernests Jansons [a], Janis Lungevics [a], Anzelms Zukuls [b], Jevgenijs Kaupuzs [b], Krisjanis Smits [c,d], Igor Velkavrh [e], Thomas Wright [e], Irina Boiko [a], Raimonds Sirants [a], Cristhian Cobas Montero [b], Tadas Malinauskas [f], Sandra Stanionyte [g], Pavels Onufrijevs [b,*]

[a] Institute of Mechanical and Biomedical Engineering, Faculty of Civil and Mechanical Engineering, Riga Technical University, Latvia
[b] Institute of Physics and Materials Science, Faculty of Natural Sciences and Technology, Riga Technical University, Latvia
[c] Institute of Solid State Physics, University of Latvia, Latvia
[d] Institute of Biomaterials and Bioengineering, Faculty of Natural Sciences and Technology, Riga Technical University, Latvia
[e] V-Research GmbH, Tribo Design Department, Dornbirn, Austria
[f] Institute of Photonics and Nanotechnology, Vilnius University, Lithuania
[g] Center for Physical Sciences and Technology, Lithuania

ARTICLE INFO

Keywords:
LIPSS
Stainless steel
Ice friction
Surface texturing
Sub-zero friction
Climate-resilient materials

ABSTRACT

The present study evaluates the frictional behaviour of nanosecond laser-induced periodic surface structures (LIPSS) formed on stainless steel *Uddeholm Ramax HH*, to investigate their sliding performance on ice. The samples were studied using surface texture analysis, contact angle measurements, Raman spectroscopy, scanning electron microscopy and X-ray diffraction. Surface analysis revealed that laser-textured samples exhibit a micro/nano-geometry with a distinctly wavy structure, complemented by low-spatial-frequency LIPSS. The results from ice friction experiments revealed a reduction in the coefficient of friction by ~ 75%, from ~ 0.20 to ~ 0.05 at low sliding velocity (0.05 m/s) for laser-irradiated surfaces and showed weak dependence within the experimental scatter on sliding velocity (range from 0.05 to 0.38 m/s) and applied normal load (range from 20 to 80 N). The reduction was attributed to the combined effects of the micro/nano LIPSS morphology and the formation of Fe_2O_3/Fe_3O_4 oxides, which lowers adhesion at the ice interface. The results demonstrate that laser-induced textures provide an efficient and environmentally friendly strategy for optimising the frictional performance of stainless steel under sub-zero conditions.

1. Introduction

One of the most complex and unexplored areas of surface optimisation is tailoring surfaces for operation under sub-zero temperatures. This challenge arises because multiple physical, chemical, and mechanical factors act simultaneously and unpredictably under such conditions. Typical examples include the prevention of icing on construction structures, tyres, road signs, wind turbines, and aeroplane wings [1,2]. Knowledge of surface modification technologies that improve friction properties can also benefit winter sports such as skiing, bobsleigh, skeleton, luge, and skating [3–6]. Conventional surface treatments often rely on environmentally hazardous chemicals to obtain the required tribological properties of engineering surfaces [7]. From a long-term perspective, such treatments are unsustainable and will eventually need to be replaced by alternative technologies.

Laser surface texturing, particularly laser-induced periodic surface structures (LIPSS), offers an environmentally friendly technology with precise and repeatable control over surface structure, morphology, and phase composition, thereby affecting properties such as wettability, adhesion, friction, and wear [8–11]. Numerous studies have shown that LIPSS can significantly alter friction and wear by creating controlled nano- and micro-textures. For example, Gnilitskyi et al. [8] found that a LIPSS textured surface for steel pair can reduce the coefficient of friction (CoF) by up to 25% and wear by up to 65% compared to an untreated surface. Murzin et al. [9] demonstrated that higher-intensity laser processing typically leads to deeper grooves and more defined surface structures, which can improve wear properties by creating micro-grooves that distribute contact stress more evenly. The study also

* Corresponding author.
E-mail address: Pavels.Onufrijevs@rtu.lv (P. Onufrijevs).

https://doi.org/10.1016/j.optlastec.2026.115253
Received 7 November 2025; Received in revised form 16 March 2026; Accepted 1 April 2026
Available online 4 April 2026

showed that LIPSS surfaces can reduce CoF by up to 35%. However, given the vast number of adjustable processing parameters (fluence, feed rate, gap width), it is not straightforward to determine the irradiation conditions that will ensure the desired friction properties.

Previous research on the interaction between laser-textured surfaces and ice or snow has yielded mixed results. Kietzig et al. [10] studied the effect of roughness and hydrophobicity on the coefficient of friction on ice by fabricating AISI304 untreated ($Ra \sim 0.6$, contact angle $\sim 84°$) and femtosecond laser-irradiated ($Ra \sim 1.1$, contact angle $\sim 128°$) samples. It was found that roughness increases friction in the boundary friction regime, while hydrophobicity directly reduces friction in the mixed/hydrodynamic regime, thereby reducing the formation of capillary bridges. Similarly, Ripamonti et al. [11] investigated methods to enhance the sliding of ski bases on snow and employed a femtosecond laser to machine symmetrical dimples (Ø35 μm, 15 μm deep) into AISI 301 stainless steel. Although the hydrophobicity of the laser-treated samples improved (from 75° to 110°), the authors noted that surface asperities generated during laser texturing neutralise the potential positive effect of hydrophobicity on sliding. More recently, Maggiore et al. [6] demonstrated that stainless steel (AISI 301) surfaces treated with ultra-short laser pulses exhibit improved frictional properties when in contact with snow, compared to untreated samples. A significant increase in the contact angle (from 80° to 130°) was measured for the laser-treated samples compared to the untreated sample, which could affect the coefficient of friction measurements, especially considering that the experiment was performed at room temperature (+15 °C). In another paper, Maggiore et al. [12] investigated the friction properties of the same material treated with LIPSS on snow at temperatures of −10, −5, and −3 °C. The average CoF for LIPSS-textured samples at −10 °C and −5 °C was observed to be only slightly lower (within the margin of error) than for the untreated sample, but decreased more notably at −3 °C (from ~ 0.09 to ~ 0.06). The authors explained this improvement as an anisotropic nano-ripple texture formed by laser processing that affects surface wettability, reducing capillary drag compared to an untreated smooth surface.

To the best of our knowledge, the tribological behaviour of nanosecond-laser-generated LIPSS on stainless steel in contact with ice has not yet been reported in the literature. Previous studies have shown that laser surface texturing can significantly increase surface hydrophobicity [6,10,13–15], which is often associated with a reduction in the coefficient of friction. In this study, nanosecond-laser-generated LIPSS are produced on Uddeholm Ramax HH steel and investigated from a multi-scale perspective that includes surface morphology, texture evolution, oxide formation, wettability, and ice tribology. The experiments are conducted over a broad range of sliding velocities and applied loads relevant to practical conditions. Particular attention is given to establishing systematic relationships between micro- and nanoscale surface texturing, laser-induced oxidation, and frictional behaviour on ice. The frictional performance is evaluated across boundary and mixed lubrication regimes, with the aim of identifying conditions that may enable velocity-independent low-friction behaviour on nanosecond-laser-textured surfaces. Therefore, this study aims to clarify how nanosecond LIPSS influence the frictional performance of stainless steel on ice as a function of laser intensity, environmental conditions, sliding velocity, and applied load.

2. Materials and methods

2.1. Preparation of the LIPSS samples

In this study, stainless steel *Uddeholm Ramax HH* (82% Fe, 13.25% Cr, 1.75% Ni, 1.49% Mn, 0.56% Mo, 0.46% C, 0.27% Si, 0.23% V, and 0.11% S) was used as the investigated material. *Uddeholm Ramax HH* is a critical material for professional winter sports, such as bobsleigh (where only this material is permitted [16]), as well as skeleton. These sports operate under severe environmental conditions, including moisture, freezing temperatures, and cyclic wet-dry exposure. The steel offers good corrosion resistance, uniform hardness, and high indentation resistance, contributing to improved durability and reliability of components used in such demanding environments. Typical industrial applications of Uddeholm Ramax HH include holders or bolsters for plastic moulds, plastic and rubber moulds with low requirements on polishability, dies for plastic extrusion, and various constructional parts.

Stainless steel Uddeholm Ramax HH rectangular shape samples (35 × 18 × 14 mm^3) were polished to a mirror-like surface with a 334 TI 15 semi-automatic polisher (Mecatech, UK). Polished samples were irradiated using a laser-induced periodic surface structuring (LIPSS) technique with a nanosecond pulsed Nd:YAG laser (NL301G, Ekspla, Lithuania) with the following parameters: wavelength 1064 nm, repetition rate of 10 Hz, pulse duration 6 ns, beam profile “Hat Top”, and laser beam diameter 1.5 mm. The laser beam diameter at the sample plane was determined using the knife-edge technique. Surface structuring was performed using a linear scanning strategy with a hatch spacing of 0.45 mm and a scanning speed of 1.25 mm s^{-1}, corresponding to approximately 70% overlap between adjacent tracks to ensure uniform surface coverage and stable LIPSS formation. Surface structuring was carried out using a straight-line hatching strategy, as illustrated in Fig. 1. The low repetition rate allows sufficient time for heat dissipation, reducing excessive surface melting and improving the reproducibility of the periodic structures. Although this repetition rate is lower than typical industrial processing conditions, it provides a controlled regime for investigating the influence of laser intensity on surface morphology and tribological behavior. The laser pulse intensity was varied at three levels: $I_1 = 237.7$ MW/cm^2, $I_2 = 385.7$ MW/cm^2, and $I_3 = 610.2$ MW/cm^2 and correspondent fluencies are shown in Table 1. The laser fluencies were chosen below the ablation threshold, which was estimated to be about 6.4 J/cm^2. This threshold value was determined as the smallest fluency at which the ablation crater appeared, as detected by the profilometry measurements. It is consistent with the known values reported for stainless steel [17]. In the text, the used intensities correspond to L1.1 (237.7) – blue, L1.2 (385.7) – green, and L1.3 (610.2) – red, respectively. The samples were irradiated at room temperature (20 ± 1 °C) and under ambient air conditions.

2.2. Sample characterization

The morphology of the samples was analysed using a high-resolution

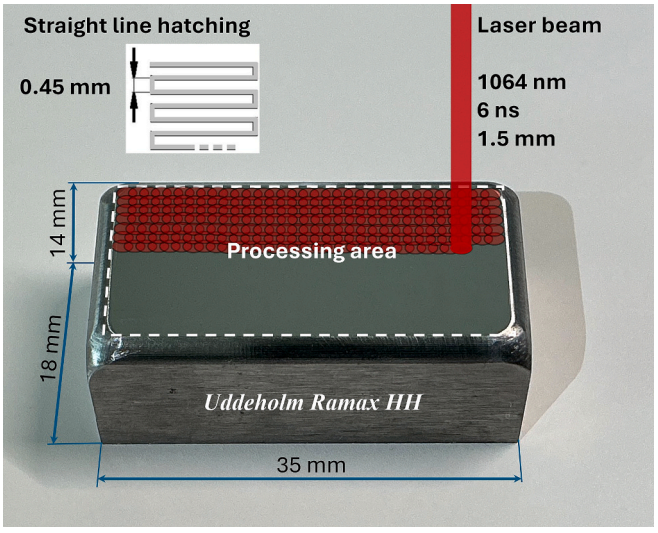

Fig. 1. Schematic representation of the linear laser scanning strategy used for surface processing, showing the hatch spacing (0.45 mm), laser parameters (1064 nm, 6 ns pulse duration, 1.5 mm beam diameter), and the processed area on the steel sample surface.

Table 1
Laser texturing parameters.

Samples	Laser pulse intensity, MW/cm^2	Laser pulse fluence, J/cm^2	Beam diameter, mm	Hatch spacing, mm	Linear speed, mm/s
L1.1 (237.7)	237.7	1.4	1.5	0.45	1.25
L1.2 (385.7)	385.7	2.3			
L1.3 (610.2)	610.2	3.7			

field emission scanning electron microscope (FESEM) equipped with focused ion beam technology (SEM-FIB, Helios 5 UX, Thermo Fisher Scientific, USA). FESEM imaging was performed at an accelerating voltage of 5 kV, utilising a high-performance in-chamber electron and ion detector (ICE) to enhance surface relief visualisation through shadowing effects and an Everhart-Thornley detector (ETD) for complementary imaging. The EDS analysis was performed in (Verios 5 UC, Thermo Fisher Scientific, USA) equipped with an Oxford X-MAX 150 EDS detector. The measurements were performed at an accelerating voltage of 20 kV and 1.6nA current.

3D surface texture measurements were performed using a contact-type profilometer Formtracer Avant FTA-H4 D3000-D (Mitutoyo, Japan). Roughness measurement parameters were based on the standard ISO 25178–3:2012 (*Geometrical Product Specifications (GPS) — Surface Texture: Areal — Part 3: Specification Operators*). The total area measured for each sample was 0.1 x 0.1 mm. Spacing for the X and Y axes was 0.1 and 0.5 μm, respectively. The S-3000 roughness detector module included a 0.75 mN detector and a stylus 12AAE882 with a cone angle of 60° and a tip radius of 1 μm. Data post-processing was performed using MCube Map Ultimate 10.0 (version 10.2.10719; Mitutoyo, Japan). All tests were conducted at 20 ± 1 °C and 42 ± 2% relative humidity.

Micro-Raman analysis was conducted at room temperature using the InVia V727 spectrometer (Renishaw, UK) in backscattering configuration. The phonon excitation was induced using a green laser (Ar^+, λ = 514.5 nm) with a grating of 1200 mm^{-1}. Each spectrum was recorded from 10 accumulations, with an exposure time of 20 s per accumulation.

Contact angle measurements were performed using the Drop Shape Analyser DSA25E (Krüss, Germany) to characterise the samples' surface wettability properties. Three measurements were conducted for each sample at room temperature (22 ± 1 °C) in air. Contact angle measurements were performed using deionised water (10.4 μl) and diiodomethane (4.5 μl) for surface energy calculations. The contact angles on the surfaces of the samples were analysed 1 month after the irradiation [18].

Structural characterisation of the samples, both before and after laser processing, was performed using X-ray diffraction (XRD). Measurements were performed using the Smartlab (Rigaku, Japan) diffractometer with a 9 kW rotating Cu anode X-ray generator. Theta/2theta scans were performed with a step size of 0.02°, and a total scan range from 30 to 90°. The obtained XRD results were analysed using the PDF 4 + database.

2.3. Ice friction tests

The modular oscillating tribometer RVM1000 (Werner Stehr Tribologie, Germany) was used. Each steel sample was mounted in an upper sample holder, allowing self-alignment in the movement direction. To prepare the ice, 18 mL of distilled water and 0.5 mL of tap water were poured into a steel bath (80 × 20 × 5 mm^3) and levelled before each test. Two ambient conditions ("cold" – air temperature 2.2 ± 0.3 °C; ice temperature −9 ± 0.2 °C; relative humidity 22 ± 3% and "warm" – air temperature 6.5 ± 0.3 °C; ice temperature −9 ± 0.2 °C; relative humidity 44 ± 2%), six sliding velocities (0.05; 0.1; 0.14; 0.19; 0.28; 0.38 m/s) and three applied normal loads (20; 50; 80 N) were used for each experiment. More information about the ice preparation and the experimental setup can be found in the work of Velkavrh et al. [19].

3. Results and discussion

3.1. FESEM

In Fig. 2, the FESEM images of the non-irradiated reference sample (Fig. 2a) and the laser-irradiated samples with laser radiation intensities of 237.7 MW/cm^2 (Fig. 1b), 385.7 MW/cm^2 (Fig. 2c), and 610.2 MW/cm^2 (Fig. 2d) are shown. The periodicity (Λ) of these structures was determined using the two-dimensional (2D) Fast Fourier Transform (FFT) method, assisted by the open-source software Gwyddion, Version 2.67 (Fig. 2e–g). To analyse the periodicity of LIPSS, the 2D-FFT profiles were examined (see profiles in supplementary material, Fig. S1). This was achieved by measuring the distance between the two most intense mirror-like related peaks, which were fitted using the Lorentz function. The formula for calculating periodicity is $\Lambda = 2/(f_1 - f_2)$, where f_1 and f_2 represent the spatial frequencies observed in the 2D-FFT profile. The periodicity of LIPSS was in the range of about Λ = 996–1027 nm, which can be classified as low spatial frequency LIPSS (LSFL) [20]. As the laser intensity increases, the ripples become more prominent and regular.

3.2. Surface texture 3D profilometry

The surface texture of LIPSS-textured surfaces and the reference surface was measured over an area of 0.1 x 0.1 mm, using the settings described in the Materials and Methods section. Fig. 3 represents the surface textures of each sample on a single scale. It is immediately apparent that, using this method for surface texture measurements, the fine LIPSS structure (visible in the FESEM images in Fig. 2) cannot be detected, but the micro-changes in the surface after laser treatment can be clearly observed. Thus, complex laser-irradiated surfaces were observed, which include changes in microgeometry and nanogeometry.

For the analysis of the descriptive parameters of the 3D surface texture listed in the standard ISO 25178–2:2021 *(Geometrical product specifications (GPS) – Surface texture: Areal – Part 2: Terms, definitions and surface texture parameters)*, four parameters were chosen that describe the surface – *Sa* (arithmetic mean height), *Sdq* (root mean square slope), *Sdr* (developed interfacial area ratio), bearing area metrics: *Sk* (core roughness depth), *Spk* (reduced peak height), *Svk* (reduced valley depth), *(Spk + Svk)/Sk* (balance ratio). These parameters were selected based on their potential correlation with tribological and wettability properties. The mentioned parameters were calculated from the measured primary surfaces and are presented in Table 2.

Surface texture parameter *Sa* is often used in industry and science to characterise surface roughness. It is generally assumed that a lower *Sa* results in a smoother surface and, therefore, a lower CoF and wear since there are no high asperities in the contact [21]. However, if the surface is too smooth (Sa close to 0), in ice friction experiments, adhesive freezing, especially at low sliding velocities, could occur, thus resulting in higher friction. In contrast, hydrophobicity can be improved directly by increasing the Sa value, as the droplet's contact surface decreases [22,23]. The parameter *Sdq* describes the steepness of peaks and valleys. Higher *Sdq* indicates steeper asperities. If *Sdq* is too high, the local stress concentration at asperity tips during contact increases, promoting ploughing, especially under higher pressure. On the other hand, if *Sdq* is low, it, like low *Sa*, can lead to the formation of capillary bridges and increased adhesion between the sample surface and the liquid-like layer on the ice surface. Suppose the optimal Sdq value can be found. In that case, it is theoretically possible to ensure drainage of meltwater during

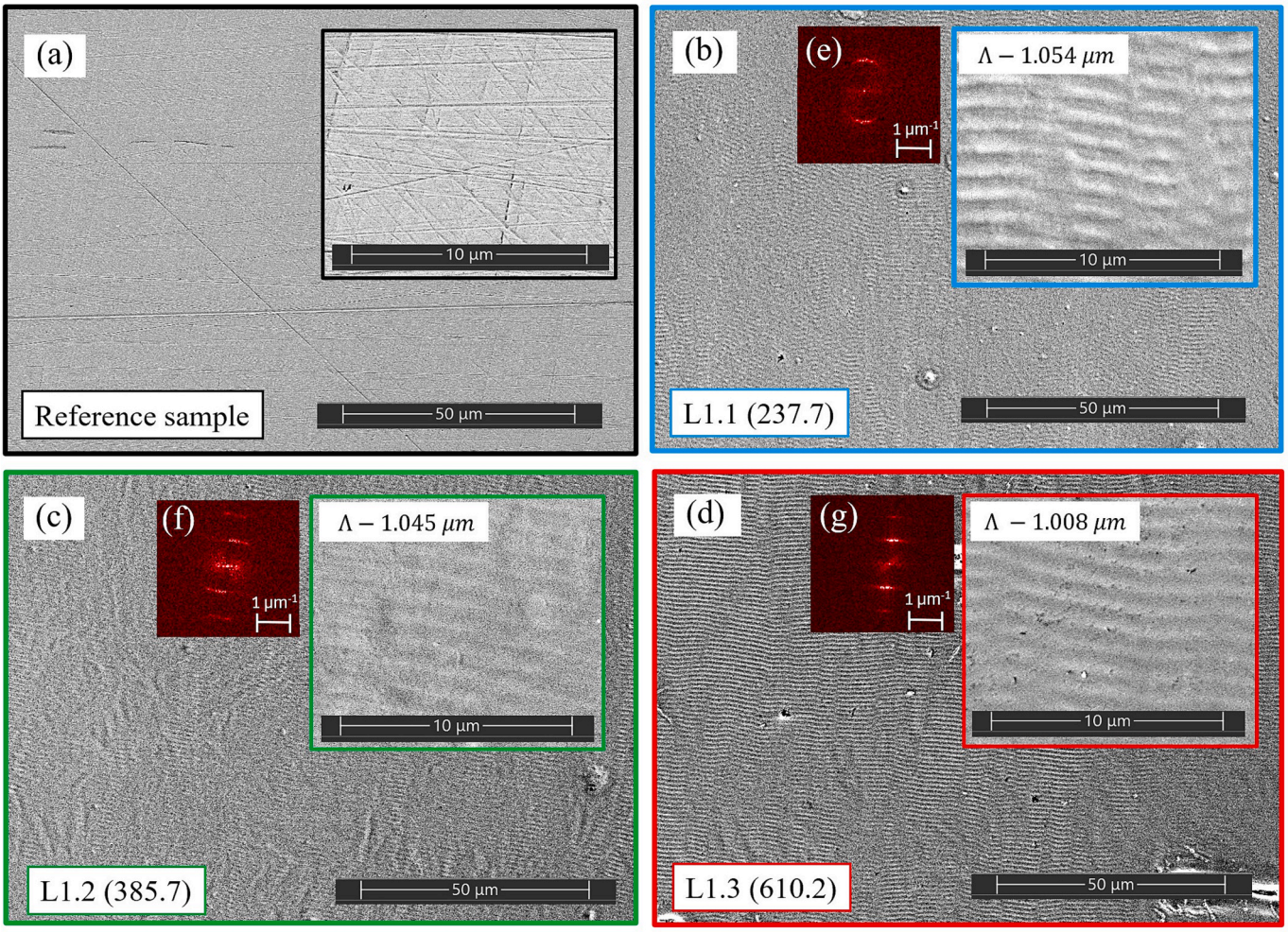

Fig. 2. FESEM images of reference and laser-irradiated samples. (a) Reference sample (non-irradiated) – black; (b) L1.1 (237.7) – blue; (c) L1.2 (385.7) – green; (d) L1.3 (610.2) – red. In brackets, laser intensity is represented in MW/cm^2. Insets (e–g) show 2D-FFT obtained from corresponding FESEM images.

sliding and to prevent excessive asperity penetration into the ice surface. *Sdr* indicates the relative increase in surface area due to texture and can separate surfaces with similar amplitude parameters [21]. Theoretically, the larger the parameter *Sdr*, the larger the actual contact area at higher contact pressure, which can enhance friction and adhesion in freezing conditions. However, if *Sdr* is optimal, meltwater can accumulate and provide additional lubrication [21,24].

If bearing curve parameters are analysed, sample L1.3 exhibits the highest core roughness depth (S_k0.17 μm) and significantly larger peak and valley components (S_{pk}0.091 μm, S_{vk}0.055 μm) compared with the other surfaces. Consequently, the relative contribution of surface features outside the core region $(S_{pk} + S_{vk})/S_k$ was also greatest for L1.3, indicating a texture dominated by pronounced asperities and valleys [21]. Theoretically, as with the other surface texture parameters considered, the bearing curve parameters also suggest that laser-textured complex surfaces with distinctly higher peaks could provide lower friction at slow sliding velocities and low applied loads. In contrast, smoother surfaces could provide lower friction precisely under the opposite conditions.

It should be emphasised that the stylus-based profilometer cannot resolve nanoscale LIPSS features due to the tip radius and sampling resolution. Therefore, the calculated ISO 25178–2:2021 parameters describe primarily the micro-scale surface modification induced by laser processing. The nanoscale LIPSS morphology is instead captured by SEM analysis (see Fig. 2) and contributes indirectly to wettability and adhesion. Consequently, correlations between ISO texture parameters and friction should be interpreted as describing micro-scale contributions to tribological behaviour.

3.3. Raman spectroscopy

Typically, Raman spectroscopy inherently exhibits low efficiency on pure metal surfaces due to metals' high reflectivity and refractive properties [25], which severely restricts the interaction volume for inelastic scattering. Conversely, forming metal oxide layers leads to the appearance of a strong Raman signal. Micro-Raman spectra for non-irradiated (reference sample) and laser-irradiated stainless steel with LIPSS are shown in Fig. 4. L1.1 exhibited the lowest Raman signal across all samples, indicating non-to-minimal oxide formation. The metal surface with the lowest laser-intensity modification exhibits a weak maximum at 678 cm^{-1}, which is attributed to the Fe–O vibration within magnetite (Fe_3O_4) [26]. In contrast, samples L1.2 and L1.3 indicate pronounced bands at a 400–750 cm^{-1} range, which correspond to hematite (Fe_2O_3) 610 cm^{-1} (E_g) and magnetite (Fe_3O_4) 660 cm^{-1} (A_{1g}) Raman active modes [27,28]. The increased intensity of the observed Raman bands at higher laser irradiation levels indicates more substantial oxide layer formation. Higher laser irradiation intensity generally correlates with higher Raman intensity [29], most noticeably for samples L1.2 and L1.3. This indicates structural or compositional changes, such as iron oxide formation, occur on the sample surface at the higher laser energy exposure. SEM–EDS results confirm an increase in oxygen content (see EDS results in supplementary material, Fig. S2-S5); however,

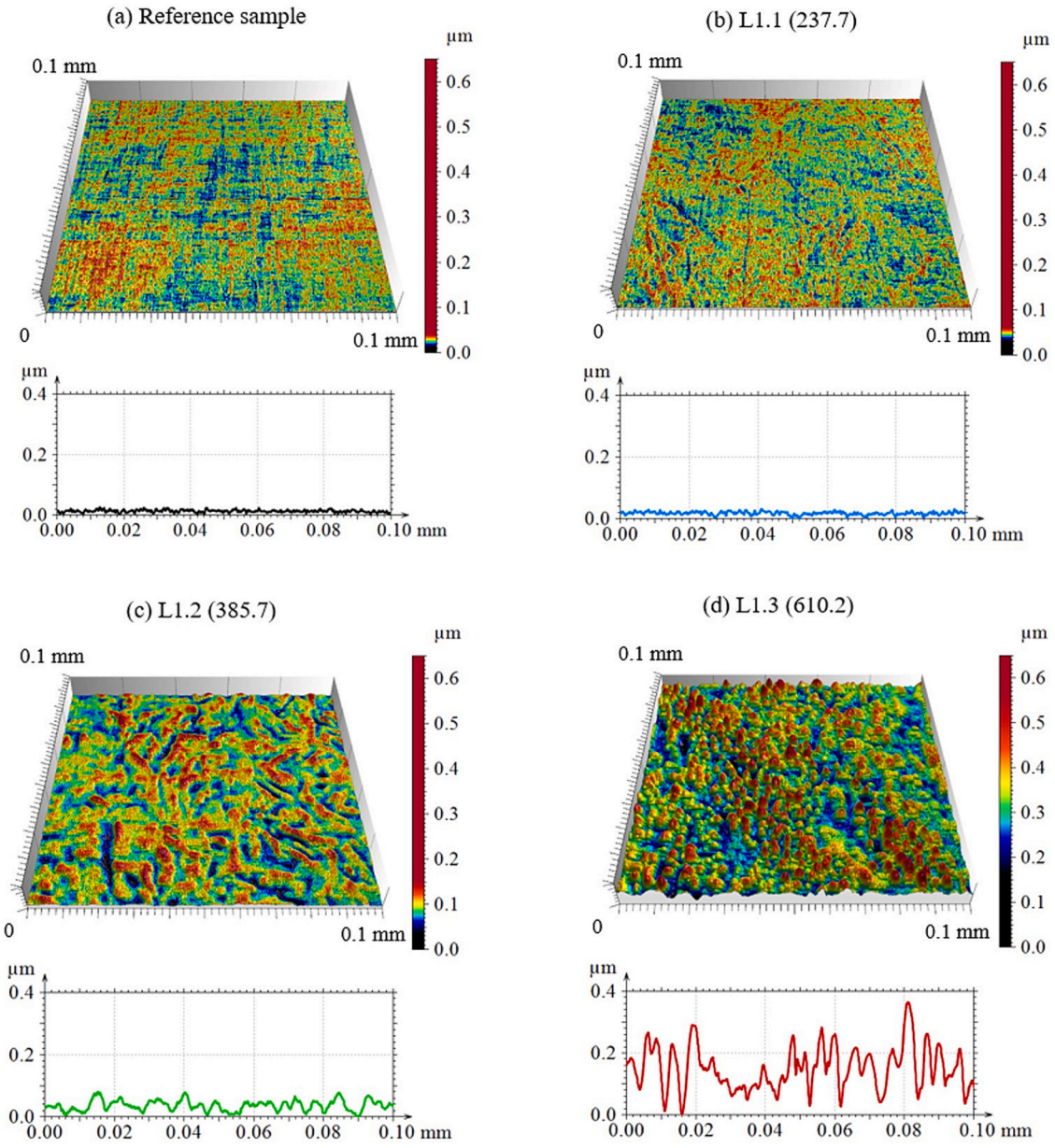

Fig. 3. Surface texture measurements (0.1 x 0.1 mm) and respective 2D profiles. (a) Reference sample (non-irradiated) – black; (b) L1.1 (237.7) – blue, (c) L1.2 (385.7) – green, (d) L1.3 (610.2) – red. In brackets, laser intensity is represented in MW/cm^2.

Table 2
Surface texture parameters.

Sample label (laser intensity, MW/cm^2)	Surface texture parameters						
	Sa (µm)	*Sdq*	*Sdr* (%)	*Sk*	*Spk*	*Svk*	*(Spk + Svk)/ Sk*
Reference sample	0.004	0.020	0.021	0.014	0.005	0.005	0.714
L1.1 (237.7)	0.004	0.022	0.024	0.014	0.006	0.005	0.786
L1.2 (385.7)	0.016	0.030	0.046	0.051	0.022	0.021	0.843
L1.3 (610.2)	0.054	0.105	0.547	0.170	0.091	0.055	0.859

due to overlapping fluorescence bands, absolute quantitative determination is not possible. In addition to iron oxides, the participation of alloying elements such as chromium in oxide formation cannot be excluded during nanosecond laser processing. However, possible Cr-rich oxides or mixed Fe–Cr spinel phases were not clearly resolved in the Raman spectra, likely due to their low concentration and the overlap with dominant iron oxide bands [30].

3.4. X-ray diffraction

X-ray diffraction (XRD) 2 θ/θ measurements reveal three peaks at 44.6°, 65.0°, and 82.0°, corresponding to the (110), (200), and (211) reflections of iron (PDF card No. 00–006-0696) [31] (see Fig. 5). The reference sample exhibits diffraction peaks at slightly lower diffraction angles, indicating a larger lattice parameter in the investigated steel than in pure iron. This shift can be attributed to the presence of alloying elements (impurities) such as Cr, Ni, Mn, Mo, C, Si, V, and S in the stainless steel matrix. Laser irradiation of the steel results in an increase in 2 θ for all observed reflections, indicating a decrease in the lattice constant with increasing laser pulse intensity. The shift of diffraction peaks toward positions characteristic of pure iron indicates a change in the lattice parameter after laser irradiation, which may be associated

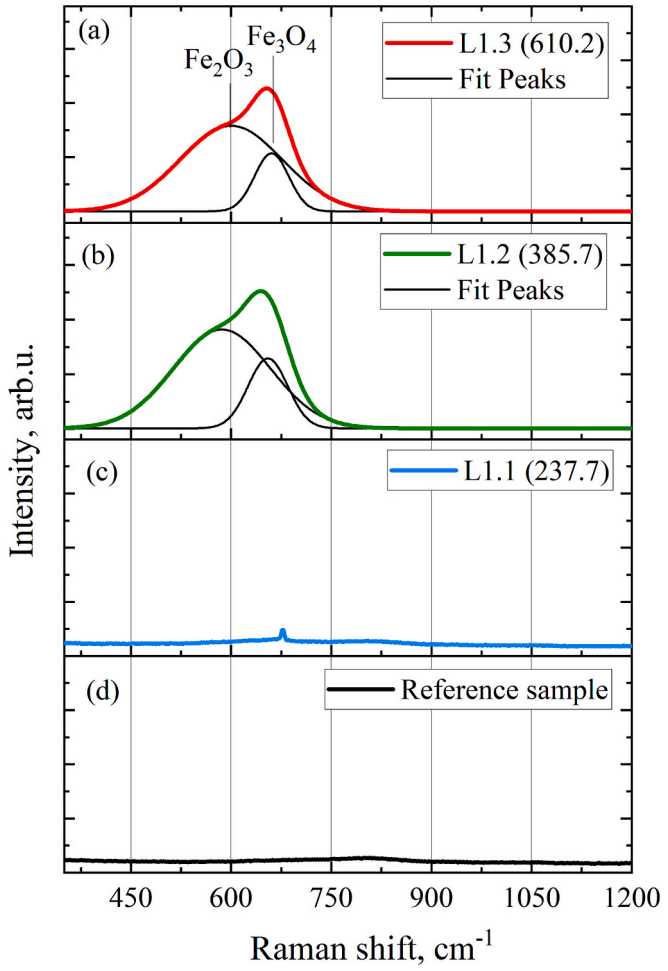

Fig. 4. Raman spectra. (a) L1.3 (610.2) – red; (b) L1.2 (385.7) – green, (c) L1.1 (237.7) – blue, (d) Reference sample (non-irradiated) – black. In brackets, laser intensity is represented in MW/cm^2.

with redistribution of alloying elements or variation of residual stresses. This effect occurs within a few micrometres of depth, as 2 θ/θ measurements provide structural information from this region.

To obtain information from the sample surface layer, grazing incidence X-ray diffraction (GI-XRD) was employed with an incidence angle of 0.3°. The resulting diffractograms, presented in Fig. 6, are plotted on a semilogarithmic scale to enhance the visibility of weak diffraction peaks. In addition to the iron diffraction peaks (PDF card No. 00–006-0696), two broad and weak peaks are observed at approximately 35° and 63°. These peaks can be attributed to Fe_3O_4 (PDF card No. 04–018-0091) or Fe_2O_3 (PDF card No. 04–016-4345), confirming the formation of both phases identified in Raman measurements [32,33].

3.5. Wettability and surface energy

Laser-induced wettability control has been widely investigated, particularly for femtosecond laser processing [29,34], where the contact angle can be tuned over a broad range. In the present study, our focus was on the formation of laser-induced periodic surface structures (LIPSS) using a nanosecond laser. The wettability measurements were performed one month after laser processing to allow stabilization of the surface chemistry. Laser-irradiated samples showed a slightly higher contact angle (up to 80.5 ± 2° water contact angle) than the non-irradiated reference sample (68.4 ± 1° water contact angle). Overall, as the laser intensity increases, the contact angle increases slightly (see Table 3). This could be explained by the rise in micro- and nano-level roughness of the surface texture at higher laser intensity, as well as the chemical changes, which accordingly enhance water-repelling properties through the Cassie-Baxter effect [35]. Additionally, when calculating the surface free energy, a decrease of approximately 10% is observed, which, in theory, may affect ice friction results at low sliding velocities, where adhesion forces between the sample and ice surfaces predominate. Additional measurements of the contact angle performed immediately after irradiation showed slightly lower values (by up to ~ 5°), indicating only minor ageing effects over time. This stabilization is likely associated with the formation of laser-induced oxide layers and subsequent surface passivation typical for nanosecond laser processing of stainless steel [36].

3.6. Ice friction tests

Ice friction tests were conducted according to the experimental settings described in the Materials and Methods section. In the experiments, the sliding velocity was increased from 0.05 m/s to 0.38 m/s, then decreased stepwise back to the initial value. Therefore, the

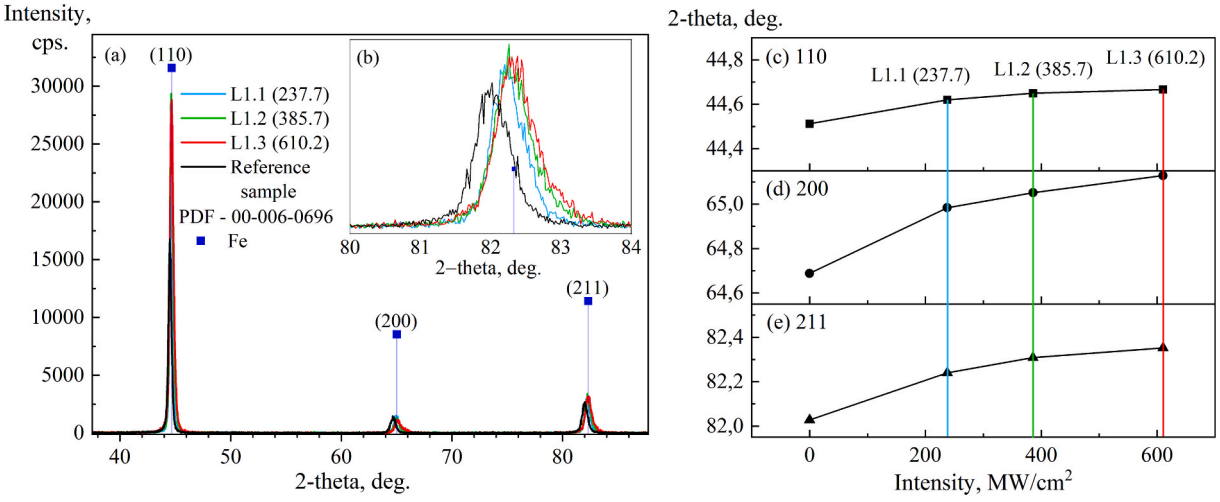

Fig. 5. XRD 2 θ/θ measurements. (a) XRD 2 θ/θ diffractograms measured in samples with various irradiation intensities. Vertical lines show reflection for the pure iron PDF card No.: 00–006-0696; (b) In the inset (211) reflections are shown; (c-e) The peak positions of (110), (200), and (211) reflections obtained from Gaussian fit for samples with various irradiation. L1.1 (237.7) – blue, L1.2 (385.7) – green, L1.3 (610.2) – red, Reference sample (non-irradiated) – black. In brackets, laser intensity is represented in MW/cm^2.

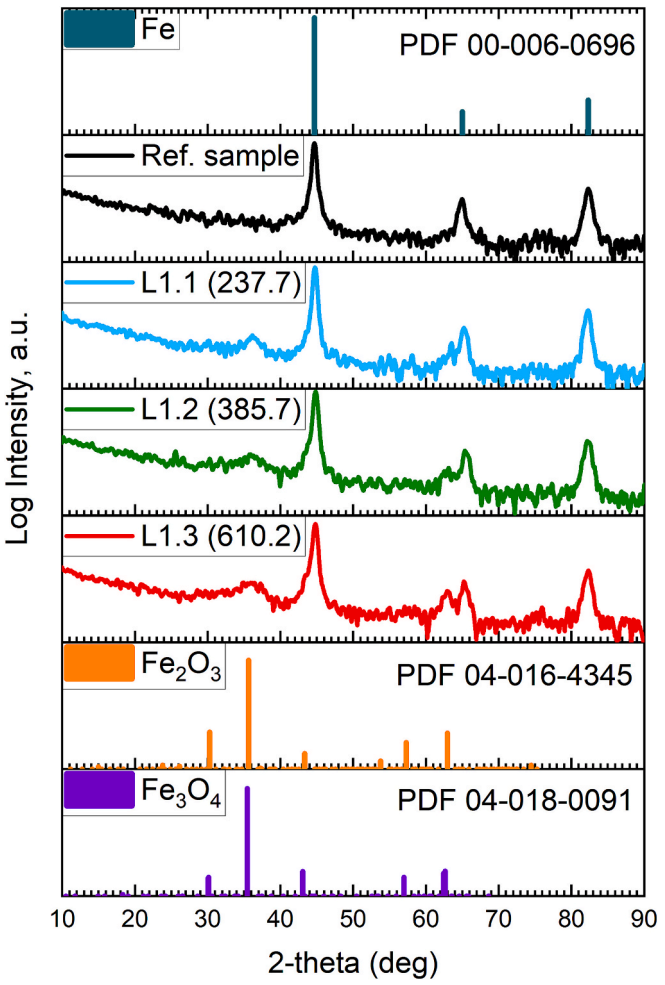

Fig. 6. Grazing-incidence XRD diffractograms of the reference and laser-irradiated samples. From top to bottom: reference sample (black), L1.1 (237.7) – blue, L1.2 (385.7) – green, L1.3 (610.2) – red. In brackets, laser intensity is represented in MW/cm^2. Vertical markers correspond to the reference diffraction peaks of Fe (PDF 00–006-0696), Fe_2O_3 (PDF 04–016-4345), and Fe_3O_4 (PDF 04–018-0091).

Table 3
Wettability and Surface energy performed one month after laser processing.

	Reference sample	L1.1 (237.7)	L1.2 (385.7)	L1.3 (610.2)
Water contact angle, °	68.4 ± 1	72.3 ± 1.5	72.7 ± 1.3	80.5 ± 2.0
Diiodomethane contact angle, °	49.4 ± 0.1	51.6 ± 1.2	46.2 ± 2.3	47.0 ± 2.4
Surface free energy, mN/m	44.4 ± 0.6	41.6 ± 1.4	43.5 ± 1.9	40.0 ± 2.1

horizontal axes in Fig. 7 and Fig. 8 are presented symmetrically so that the mean sliding velocity first increases and then decreases. Each experiment was performed at three applied loads (20, 50 and 80 N) to analyse the effect of load on the friction properties. Each data point in the friction plots represents the average CoF calculated from at least 20 individual measurements. The error bars indicate the corresponding standard deviation. While Figs. 7 and 8 show results from a single representative experiment under the specified experimental conditions, multiple replicate tests were conducted, all of which showed the same trend in CoF, confirming the consistency of the observed behaviour. Measurements were also performed under two environmental conditions, thus simulating "warm" and "cold" conditions. Fig. 7 represents the coefficient of friction results for each tested sample ((a) Reference sample; (b) L1.1 (237.7), (c) L1.2 (385.7), (d) L1.3 (610.2)) under the above-described conditions.

The ice friction curves of the polished reference sample ((a) Reference sample Fig. 7) obtained under both "cold" and "warm" conditions exhibit the characteristic behaviour commonly reported for ice friction: the CoF decreases with increasing sliding velocity. Furthermore, the CoF tends to be lower at elevated temperatures and humidity levels [37–39]. If applied loads are analysed, a higher applied load results in a lower CoF, a typical ice friction characteristic as well [39,40], supporting the adequacy of the experimental settings and conditions. The laser-textured sample L1.1 (237.7), treated with the lowest laser intensity, still exhibits dependency on sliding velocity at "cold" ambient conditions that is comparable to the reference (untreated) sample. However, lower coefficient of friction values can be observed at lower sliding velocities (up to 0.1 m/s). In contrast, for samples L1.2 and L1.3, the effect of applied load and velocity on the coefficient of friction is minor. Nevertheless, the laser-textured surfaces consistently exhibit a substantially reduced CoF value compared to the untreated sample, particularly under "cold" conditions and at low sliding velocities (up to a threefold reduction). At higher velocities (0.38 m/s), the CoF values are nearly identical for all samples. This behaviour may result from the stick–slip phenomenon, where the polished surface adheres to the liquid-like layer on the ice surface due to capillary forces [39,41].

Fig. 8 presents a 3D plot of the coefficient of friction as a function of sliding velocity and laser intensity at the three considered applied loads (20, 50 and 80 N) and two ambient conditions ("warm" and "cold"), thus making it possible to directly compare how the curve character and coefficient of friction change for the untreated reference sample and the laser-textured samples.

Analysis of the curved profiles (see Fig. 8) indicated that the CoF for the laser-textured samples L1.2 and L1.3 appears to be less sensitive to sliding velocity (variations up to 28%) and applied load (up to 35% for L1.2 and 19% L1.3) under the investigated experimental settings. In contrast, the polished reference sample exhibits a significant dependence of CoF on both sliding velocity (up to an 81% variation) and applied load (up to a 48% variation), particularly under "cold" ambient conditions that correspond to the boundary friction regime [19,39]. Thus, as the applied load and sliding velocity increase, a thicker, liquid-like layer forms, enhancing lubrication and thereby reducing the coefficient of friction. Sample L1.1 also displays a dependence of the coefficient of friction on sliding velocity (up to 56%) and applied load (up to 49%), although within a comparatively lower range. As demonstrated by Raman and XRD measurements, minimal Fe_3O_4 oxide was formed on the surface of sample L1.1 after laser irradiation. In contrast, for samples L1.2 and L1.3, Fe_2O_3 oxide already dominates the surface layer.

As it is known, at low sliding velocities, friction is primarily governed by adhesive interactions between the ice and the solid surface [39,42]. Under these conditions, smoother surfaces (Reference sample and L1.1) provide a larger real contact area, promoting stronger adhesive bonding and resulting in higher friction. In contrast, the rougher L1.2 and L1.3 surfaces are characterised by their high S_k and S_{pk} values, presents fewer real contact points under low load, thereby reducing ice adhesion and yielding the lowest coefficient of friction in these settings.

As the sliding velocity increases, frictional heating becomes significant, leading to the formation of a thin melt layer at the interface. Adhesion plays a diminished role, and friction is increasingly controlled by viscous shearing within the melt film. In such situations, ploughing between surface asperities and the ice surface may occur, increasing friction. Smoother surfaces mitigate the possible ploughing effect. As a result, the differences in friction between the tested surfaces become less pronounced, and in some cases, the reference surface even exhibits slightly lower friction than the laser-textured ones.

The correlation between the coefficient of friction and the surface texture parameter $(Spk+Svk)/Sk$ is presented in Fig. 9 for the highest

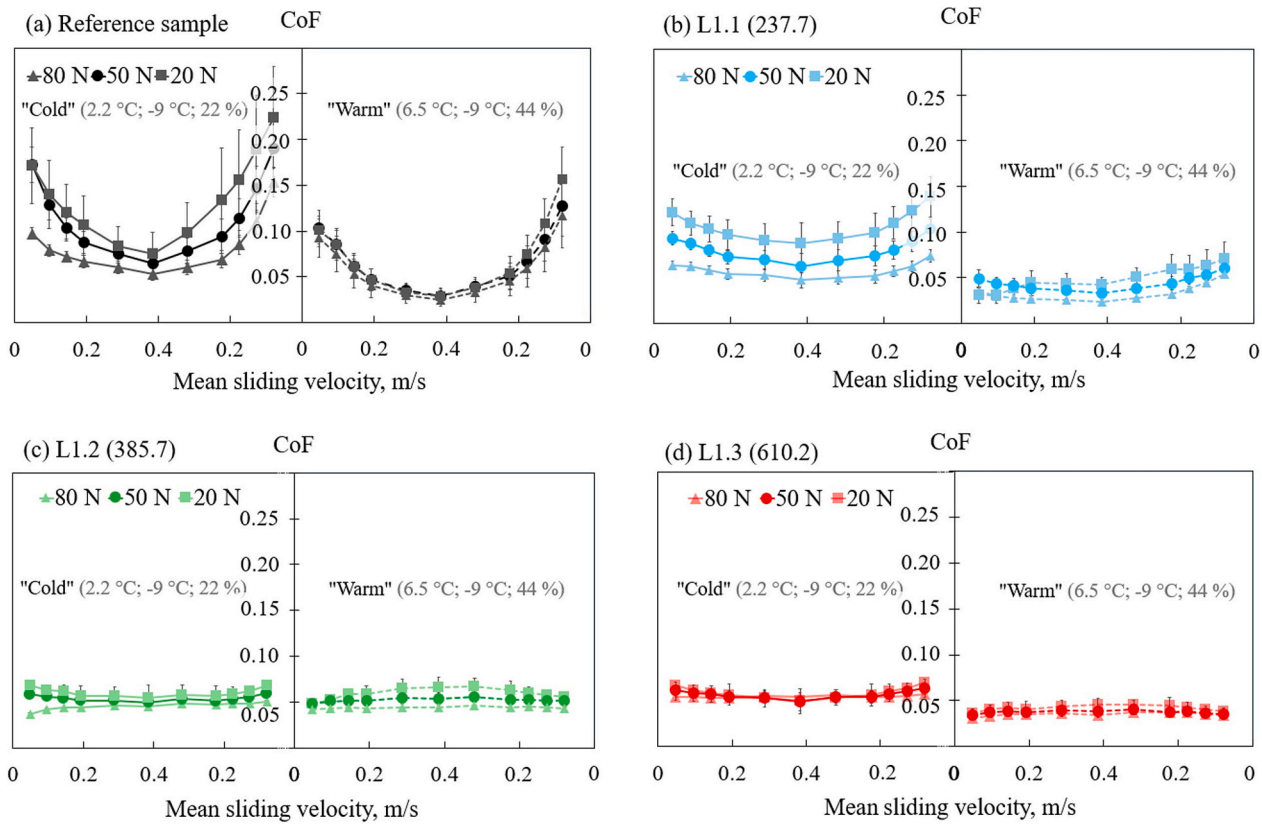

Fig. 7. Ice friction results for each sample, depending on sliding velocity, applied load, and ambient conditions. (a) Reference sample; (b) L1.1 (237.7), (c) L1.2 (385.7), (d) L1.3 (610.2). In brackets, laser intensity is represented in MW/cm^2.

and lowest loads (20 and 80 N) and sliding velocities (0.05 and 0.38 m/s) under cold and warm ice conditions. The combined parameter $(Spk+Svk)/Sk$ was selected for clarity of interpretation, as it provides a balanced representation of peak and valley contributions relative to the core roughness. Compared with individual roughness parameters (e.g., Sa; see Table 2), the distribution of this parameter is more compact and does not contain isolated outlying values that would disproportionately influence the correlation.

Under cold conditions, a consistent negative correlation is observed, indicating that increasing surface complexity reduces friction for both loads and velocities. This behaviour is characteristic of an adhesion-controlled regime, where enhanced microtexture reduces the real contact area and weakens ice adhesion. A similar trend is observed under warm conditions at the lower sliding velocity (0.05 m/s), suggesting that adhesion remains the dominant friction mechanism at low speed. In contrast, at the higher sliding velocity (0.38 m/s) under warm conditions, the trend reverses, and smoother surfaces exhibit lower friction. This transition marks the onset of a melt-lubricated regime, in which frictional heating promotes the formation of a lubricating water film at the interface. Under these conditions, pronounced micro-roughness is likely to increase ploughing of the softened ice surface and disrupt the stability of the water film, resulting in higher friction. The observed correlations, therefore, quantitatively support the transition from adhesion-dominated to melt-lubricated friction with increasing temperature and sliding speed.

The influence of laser structuring on CoF on ice arises from: (1) chemical changes in the material, as demonstrated by the Raman Spectra (see Fig. 4) and XRD (see Fig. 5; 6) results, and (2) surface texture changes, which are visible in the surface texture measurements (see Fig. 3) and FESEM images (see. Fig. 2). It is known that the oxide layer, due to its chemical properties and reduced adhesion, can reduce friction under dry sliding conditions [43–45]. Additionally, in snow, oxide flakes reduce friction [46]. The oxide layer may reduce the adhesion between the steel surface and the liquid-like layer, thus decreasing the capillary force [39,47]. In this case, laser texturing produces a complex surface texture that exhibits a dual nature, depending on the friction regime. The ice friction results indicate a transition from an adhesion-controlled regime at low velocities—where rougher, peak-dominated textures minimise ice adhesion—to a melt-lubricated regime at higher velocities and applied loads, where smoother surfaces promote more stable lubrication and mitigate the ploughing effect.

Although only a slight reduction (up to 10%) in surface energy was measured, its effect on the coefficient of friction cannot be completely ruled out, particularly at low sliding velocities where adhesive forces play a larger role in the interaction between the steel and ice surfaces. Overall, the findings indicate that the frictional behaviour of LIPSS-textured stainless steel on ice surfaces is mainly influenced by surface texture and chemical changes, as well as lubrication, rather than by significant alterations in wettability.

From an industrial perspective, laser texturing offers a scalable and environmentally friendly alternative to conventional chemical anti-icing treatments and coatings, eliminating the use of hazardous chemicals and significantly reducing waste generation and water consumption compared with chemical etching or coating processes. Compared with abrasive or mechanical treatments, which may require 3–5 kWh m^{-2} [48,49] to achieve similar surface modification, reported values for laser texturing indicate that laser microtexturing typically consumes about 0.5–2 kWh m^{-2} [50–52], depending on the processing parameters. The relatively low repetition rate used in this study was chosen to ensure controlled LIPSS formation; however, for industrial implementation, higher repetition rates and multi-beam processing strategies could be employed to substantially increase processing speed and treated area coverage.

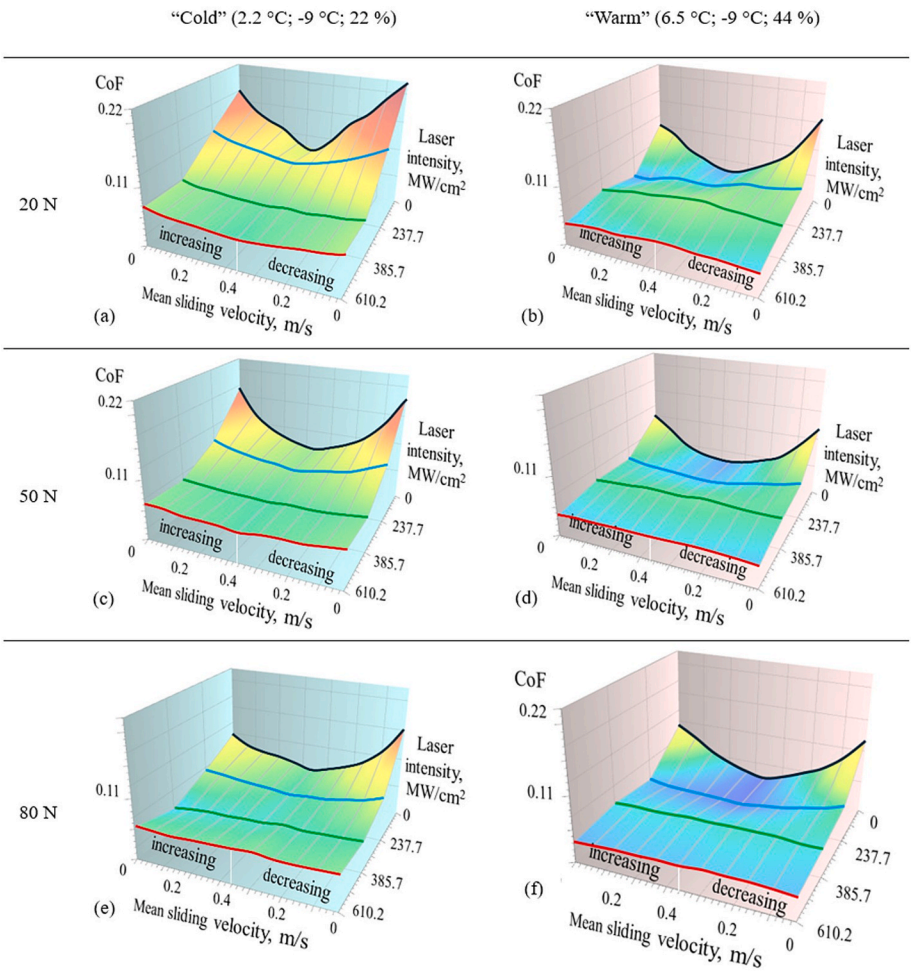

Fig. 8. Ice friction 3D plot – dependence of the CoF on sliding velocity and laser intensity at two ambient conditions and three applied loads. (a; c; e) "Cold" ambient conditions; (b; d; f) "Warm" ambient conditions. L1.1 (237.7) – blue line, L1.2 (385.7) – green line, L1.3 (610.2) – red line, Reference sample (non-irradiated) – black line. In brackets, laser intensity is represented in MW/cm^2.

4. Conclusions

For the first time, a structured study was conducted analysing the friction properties of stainless steel surfaces treated with LIPSS laser technology at various laser intensities ($I_1 = 237.7$ MW/cm^2, $I_2 = 385.7$ MW/cm^2, and $I_3 = 610.2$ MW/cm^2) on an ice surface under varying loads (20, 50, 80 N), sliding velocities (0.05; 0.1; 0.14; 0.19; 0.28; 0.38 m/s), and ambient conditions ("cold" – air temperature 2.2 ± 0.3 °C; ice temperature -9 ± 0.2 °C; relative humidity 22 ± 3% and "warm" – air temperature 6.5 ± 0.3 °C; ice temperature -9 ± 0.2 °C; relative humidity 44 ± 2%). As a result, LIPSS formation on stainless steel surfaces significantly enhances their frictional performance on ice at low sliding velocities. The LIPSS-textured surface achieved an average CoF of $\sim$ 0.05 compared to $\sim$ 0.20 for the non-irradiated sample (reference). However, as the sliding velocity increases, the differences in the coefficient of friction on ice between the LIPSS textured samples and the reference sample become negligible.

The structural and chemical surface changes induced by laser irradiation, in particular the formation of oxide layers such as Fe_2O_3 and Fe_3O_4, were confirmed by XRD and Raman spectroscopy. These oxide layers became more pronounced as laser energy increased. Performing laser processing under atmospheric conditions is beneficial because it simplifies the procedure and is particularly useful for processing large or geometrically complex components.

For samples treated with higher laser intensities, a dual micro/nano geometry change was observed, where both larger irregularities were formed (Samples L1.2; L1.3), as measured by surface 3D texture analysis, and the typical LIPSS structure, which was observed in FESEM images. Contact angle and surface energy measurements indicated relatively minor changes (up to 10%) between the reference sample and the laser-textured samples; therefore, it can be concluded that, in this case, the friction properties on ice were not primarily affected by changes in wettability, but rather by changes in surface geometry.

These findings strongly suggest that laser texturing, as a clean and environmentally friendly method, can be utilised to enhance surface performance under specific conditions without introducing external contaminants.

CRediT authorship contribution statement

Armands Leitans: Writing – review & editing, Writing – original draft, Visualization, Investigation, Conceptualization. **Ernests Jansons:** Writing – review & editing, Writing – original draft, Visualization, Methodology, Investigation, Conceptualization. **Janis Lungevics:** Writing – review & editing, Visualization, Methodology, Investigation, Conceptualization. **Anzelms Zukuls:** Writing – review & editing, Visualization, Investigation. **Jevgenijs Kaupuzs:** Investigation. **Krisjanis Smits:** Investigation. **Igor Velkavrh:** Writing – review & editing, Investigation. **Thomas Wright:** Writing – review & editing. **Irina Boiko:** Writing – review & editing. **Raimonds Sirants:** Visualization, Investigation. **Cristhian Cobas Montero:** Investigation. **Tadas Malinauskas:** Investigation. **Sandra Stanionyte:** Investigation. **Pavels**

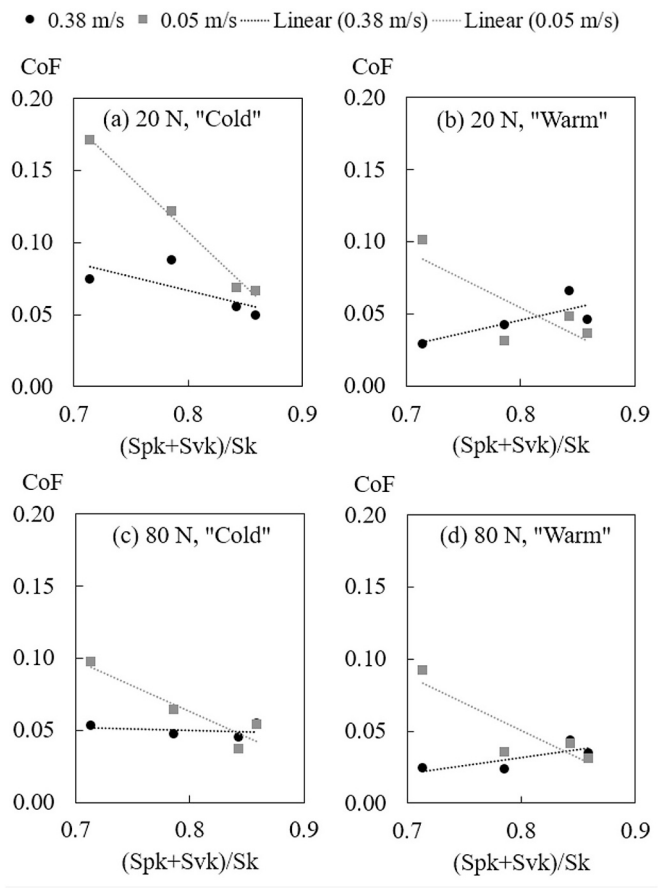

Fig. 9. Correlation between coefficient of friction (CoF) and the surface texture parameter $(Spk+Svk)/Sk$ under "cold" and "warm" ambient conditions at applied loads of 20 N (a, b) and 80 N (c, d) and sliding velocities of 0.05 and 0.38 m/s.

Onufrijevs: Writing – review & editing, Visualization, Supervision, Project administration, Methodology, Funding acquisition, Conceptualization.

Declaration of competing interest

The authors declare that they have no known competing financial interests or personal relationships that could have appeared to influence the work reported in this paper.

Acknowledgements

This research is funded by the Fundamental and Applied Research project "Innovative Multifunctional Laser-Textured Surfaces with Improved Tribological Performance and Icephobicity" (lzp-2023/1-0060), Latvia. IV and TW have been supported by the Austrian COMET-Program (project InTribology2, No. 906860, project coordinator AC2T research GmbH). The authors thank Mitutoyo Poland Sp.o.o. for providing Formtracer Avant FTA - H4 D3000-D.

Appendix A. Supplementary data

Supplementary data to this article can be found online at https://doi.org/10.1016/j.optlastec.2026.115253.

Data availability

Data will be made available on request.

References

[1] Y. Cao, W. Tan, Z. Wu, Aircraft icing: an ongoing threat to aviation safety, Aerosp. Sci. Technol. 75 (2018) 353–385, https://doi.org/10.1016/j.ast.2017.12.028.
[2] V. Okulov, I. Kabardin, D. Mukhin, K. Stepanov, N. Okulova, Physical de-icing techniques for wind turbine blades, Energies 14 (2021) 6750, https://doi.org/10.3390/en14206750.
[3] F. Braghin, F. Cheli, S. Maldifassi, S. Melzi, E. Sabbioni, The engineering approach to winter sports, Springer, London, 2016, 10.1007/978-1-4939-3020-3.
[4] S. Rohm, M. Hasler, C. Knoflach, J. van Putten, S.H. Unterberger, K. Schindelwig, R. Lackner, W. Nachbauer, Friction between steel and snow in dependence of the steel roughness, Tribol. Lett. 59 (2015) 27, https://doi.org/10.1007/s11249-015-0554-x.
[5] E. Jansons, J. Lungevics, K. Stiprais, L. Pluduma, K.A. Gross, Measurement of sliding velocity on ice, as a function of temperature, runner load and roughness, in a skeleton push-start facility, Cold Reg. Sci. Technol. 151 (2018), https://doi.org/10.1016/j.coldregions.2018.03.015.
[6] E. Maggiore, I. Mirza, D. Dellasega, M. Tommasini, P.M. Ossi, Sliding on snow of AISI 301 stainless steel surfaces treated with ultra-short laser pulses, Appl. Surf. Sci. Adv. 7 (2022) 100194, https://doi.org/10.1016/j.apsadv.2021.100194.
[7] Q. Li, Z. Guo, Fundamentals of icing and common strategies for designing biomimetic anti-icing surfaces, J. Mater. Chem. A 6 (2018) 13549–13581, https://doi.org/10.1039/c8ta03259a.
[8] I. Gnilitskyi, A. Rota, E. Gualtieri, S. Valeri, L. Orazi, Tribological properties of high-speed uniform femtosecond laser patterning on stainless steel, Lubricants 7 (2019), https://doi.org/10.3390/lubricants7100083.
[9] S.P. Murzin, V.B. Balyakin, G. Liedl, A.A. Melnikov, R. Fürbacher, Improving Tribological Properties of Stainless Steel Surfaces by Femtosecond Laser Irradiation, (2020) 1–12.
[10] A.-M. Kietzig, S.G. Hatzikiriakos, P. Englezos, Ice friction: the effects of surface roughness, structure, and hydrophobicity, J. Appl. Phys. 106 (2009) 024303, https://doi.org/10.1063/1.3173346.
[11] F. Ripamonti, V. Furlan, A.G. Demir, B. Previtali, M. Derai, F. Cheli, P.M. Ossi, Innovative metallic solutions for alpine ski bases, J. Vac. Sci. Technol., B: Nanotechnol. Microelectron.: Mater., Process., Meas., Phenom. 36 (2018) 01A108, https://doi.org/10.1116/1.5002542.
[12] E. Maggiore, C. Corsaro, E. Fazio, I. Mirza, F. Ripamonti, M. Tommasini, P.M. Ossi, Laser-treated steel surfaces gliding on snow at different temperatures, Materials (basel). 16 (2023) 3100, https://doi.org/10.3390/MA16083100.
[13] N.A. Nordin, P. Styring, Superhydrophobic ski bases for reduced water adhesion, Procedia Eng. 72 (2014) 605–610, https://doi.org/10.1016/j.proeng.2014.06.105.
[14] L. Kuzmin, P. Carlsson, M. Tinnsten, The relationship between the type of machining of the ski running-surface and its wettability and capillary drag, Sport. Technol. 3 (2010) 121–130, https://doi.org/10.1080/19346182.2010.538399.
[15] A. Volpe, C. Gaudiuso, A. Ancona, Laser fabrication of anti-icing surfaces: a review, Materials (basel). 13 (2020) 1–24, https://doi.org/10.3390/ma13245692.
[16] B. Grzemba, R. Pohrt, Ice-versus-steel friction: an advanced numerical approach for competitive winter sports applications, Lubricants 12 (2024) 203, https://doi.org/10.3390/lubricants12060203.
[17] J.G.A.B. Simões, R. Riva, W. Miyakawa, High-speed Laser-Induced Periodic Surface Structures (LIPSS) generation on stainless steel surface using a nanosecond pulsed laser, Surf. Coatings Technol. 344 (2018) 423–432, https://doi.org/10.1016/j.surfcoat.2018.03.052.
[18] V. Kumar, R. Verma, S. Kango, V.S. Sharma, Recent progresses and applications in laser-based surface texturing systems, Mater. Today Commun. 26 (2021) 101736, https://doi.org/10.1016/j.mtcomm.2020.101736.
[19] L. Velkavrh, Jansons Klien, Ausserer Voyer, The influence of isotropic surface roughness of steel sliders on ice friction under different testing conditions, Lubricants 7 (2019) 106, https://doi.org/10.3390/lubricants7120106.
[20] J. Bonse, S.V. Kirner, J. Krüger, Laser-induced periodic surface structures (LIPSS), in: Handb. Laser Micro- Nano-Engineering, Springer International Publishing, Cham, 2021, pp. 1–59, https://doi.org/10.1007/978-3-319-69537-2_17-2.
[21] P. Pawlus, R. Reizer, M. Wieczorowski, Functional importance of surface texture parameters, Mater. (basel, Switzerland) 14 (2021), https://doi.org/10.3390/MA14185326.
[22] X. Wang, Q. Zhang, Role of surface roughness in the wettability, surface energy and flotation kinetics of calcite, Powder Technol. 371 (2020) 55–63, https://doi.org/10.1016/J.POWTEC.2020.05.081.
[23] Q. Du, P. Zhou, Y. Pan, X. Qu, L. Liu, H. Yu, J. Hou, Influence of hydrophobicity and roughness on the wetting and flow resistance of water droplets on solid surface: a many-body dissipative particle dynamics study, Chem. Eng. Sci. 249 (2022) 117327, https://doi.org/10.1016/J.CES.2021.117327.
[24] J. Berglund, C.A. Brown, B.G. Rosén, N. Bay, Milled die steel surface roughness correlation with steel sheet friction, CIRP Ann. 59 (2010) 577–580, https://doi.org/10.1016/J.CIRP.2010.03.140.
[25] W. Ji, B. Zhao, Y. Ozaki, Semiconductor materials in analytical applications of surface-enhanced Raman scattering, J. Raman Spectrosc. 47 (2016) 51–58, https://doi.org/10.1002/JRS.4854.
[26] M. Ortiz-Morales, C. Frausto-Reyes, J.J. Soto-Bernal, S.E. Acosta-Ortiz, R. Gonzalez-Mota, I. Rosales-Candelas, Infrared nanosecond pulsed laser irradiation of stainless steel: Micro iron-oxide zones generation, Spectrochim. Acta - Part A Mol. Biomol. Spectrosc. 128 (2014) 681–685, https://doi.org/10.1016/j.saa.2014.02.201.
[27] X.F. Qu, Q.Z. Yao, G.T. Zhou, S.Q. Fu, J.L. Huang, Formation of hollow magnetite microspheres and their evolution into durian-like architectures, J. Phys. Chem. C

114 (2010) 8734–8740, https://doi.org/10.1021/JP912278R/ASSET/IMAGES/MEDIUM/JP-2009-12278R_0001.GIF.
[28] J.M.J. Santillán, D. Muñetón Arboleda, D.F. Coral, M.B. Fernández van Raap, D. Muraca, D.C. Schinca, L.B. Scaffardi, Optical and magnetic properties of Fe nanoparticles fabricated by femtosecond laser ablation in organic and inorganic solvents, ChemPhysChem 18 (2017) 1192–1209, https://doi.org/10.1002/CPHC.201601279.
[29] C. Berrospe-Rodriguez, B. Baskar, J. Williams, G. Aguilar, Wettability tuning on stainless steel LIPSS by laser oxidation and its implication on cavitation bubble dynamics, Appl. Surf. Sci. 672 (2024) 160803, https://doi.org/10.1016/j.apsusc.2024.160803.
[30] L. Kotsedi, V. Furlan, V. Bharadwaj, K. Kaviyarasu, B. Sotillo, C.B. Mtshali, N. Matinise, A.G. Demir, B. Previtali, R. Ramponi, S.M. Eaton, M. Maaza, Chromium oxide formation on nanosecond and femtosecond laser irradiated thin chromium films, Opt. Mater. (amst). 95 (2019) 109206, https://doi.org/10.1016/j.optmat.2019.109206.
[31] J.T. Cahill, J.P. Kelly, E. Novitskaya, M. McKee, J.A. Bahena, O.A. Graeve, Suppressing η-phase development in steel-cemented tungsten carbide: a spark plasma sintering study, J. Am. Ceram. Soc. 102 (2019) 595–601, https://doi.org/10.1111/JACE.15814.
[32] O. Yazici, S. Yilmaz, S. Yildirim, Microstructural and mechanical properties examination of high-power diode laser-treated R260 grade rail steels under different processing temperatures, Metall. Mater. Trans. A Phys. Metall. Mater. Sci. 50 (2019) 1061–1075, https://doi.org/10.1007/S11661-018-5041-1/METRICS.
[33] M. Chirita, A. Bezergheanu, C. Bazil Cizmas, A. Ercuta, Superparamagnetic-like micrometric single crystalline magnetite for biomedical application synthesis and characterization, Magnetochemistry 2023 9 (2022) 59, https://doi.org/10.3390/MAGNETOCHEMISTRY9010005.
[34] O. Varlamova, J. Reif, M. Stolz, R. Borcia, I.D. Borcia, M. Bestehorn, Wetting properties of LIPSS structured silicon surfaces, Eur. Phys. J. B 92 (2019) 91, https://doi.org/10.1140/epjb/e2019-90672-2.
[35] O. Myronyuk, E. Vanagas, A.M. Rodin, M. Wesolowski, Estimation of the structure of hydrophobic surfaces using the cassie–baxter equation, Mater 17 (2024) 4322, https://doi.org/10.3390/MA17174322.
[36] Q. Yang, H. Li, Z. Yi, J. Cheng, D. Lou, L. Chen, Q. Li, D. Liu, Nanosecond laser passivation and corrosion resistance mechanism on the surface of 2205 duplex stainless steel, Phys. Status Solidi 222 (2025) 1–12, https://doi.org/10.1002/pssa.202400438.
[37] E. Jansons, M. Irbe, K.A. Gross, Influence of weather conditions on sliding over ice at a push-start training facility, Biotribology 25 (2021), https://doi.org/10.1016/j.biotri.2020.100152.
[38] M. Scherge, R. Böttcher, A. Spagni, D. Marchetto, High-speed measurements of steel–ice friction: experiment vs calculation, Lubricants 6 (2018) 26, https://doi.org/10.3390/lubricants6010026.
[39] A.M. Kietzig, S.G. Hatzikiriakos, P. Englezos, Physics of ice friction, J. Appl. Phys. 107 (2010) 081101, https://doi.org/10.1063/1.3340792.
[40] M. Scherge, R. Bottcher, M. Richter, U. Gurgel, High-speed ice friction experiments under lab conditions: on the influence of speed and normal force, ISRN Tribol. 2013 (2013) 1–6, https://doi.org/10.5402/2013/703202.
[41] R. Rosenberg, Why is ice slippery? Phys. Today 58 (2005) 50–54, https://doi.org/10.1063/1.2169444.
[42] E. Jansons, J. Lungevics, I. Velkavrh, T. Wright, Ice friction: a brief review of the influencing factors and experimental methods, Friction 13 (2025) 9441076, https://doi.org/10.26599/FRICT.2025.9441076.
[43] X. Cheng, Z. Jiang, D. Wei, H. Wu, L. Jiang, Adhesion, friction and wear analysis of a chromium oxide scale on a ferritic stainless steel, Wear 426–427 (2019) 1212–1221, https://doi.org/10.1016/J.WEAR.2019.01.045.
[44] J. Glascott, F.H. Stott, G.C. Wood, The effectiveness of oxides in reducing sliding wear of alloys, Oxid. Met. 24 (1985) 99–114, https://doi.org/10.1007/BF00664227/METRICS.
[45] K. Hoshino, M. Nagoshi, W. Tanimoto, Y. Yamasaki, S. Furuya, A. Matsuzaki, N. Yoshimi, Effect of Al-based oxide layer on frictional properties of hot-dip galvanized steel sheets, ISIJ Int. 57 (2017) 895–904, https://doi.org/10.2355/ISIJINTERNATIONAL.ISIJINT-2016-704.
[46] Y. Lyu, E. Bergseth, U. Olofsson, Open system tribology and influence of weather condition, Sci. Reports. 61 (6) (2016) 1–11, https://doi.org/10.1038/srep32455.
[47] M. Tikanmäki, P. Sainio, Experiments on friction of dry and wet ice, Cold Reg. Sci. Technol. 172 (2020) 102990, https://doi.org/10.1016/j.coldregions.2020.102990.
[48] V. Lavrinenko, V. Solod, Analysis of available data and estimation of energy supply of mechanical processing, Mech. Adv. Technol. 6 (2022) 293–301, https://doi.org/10.20535/2521-1943.2022.6.3.267250.
[49] A.N. Alberro, H.A.G. Rojas, A.J.S. Egea, S. Hameed, R.M.P. Aguilar, Model based on an effective material-removal rate to evaluate specific energy consumption in grinding, Mater 12 (12) (2019), https://doi.org/10.3390/ma12060939.
[50] K.E. Hazzan, M. Pacella, T.L. See, Laser processing of hard and ultra-hard materials for micro-machining and surface engineering applications, Micromachines 12 (12) (2021), https://doi.org/10.3390/mi12080895.
[51] H. Martinez-Zavala, D. Bhaduri, P. Petkov, A. Valera-Medina, S. Bigot, Effects of laser microtextured surfaces in condensation heat transfer, Procedia CIRP 95 (2020) 927–932, https://doi.org/10.1016/j.procir.2020.01.184.
[52] J. Wu, C. Zhang, P. Jiang, C. Li, H. Cao, S. Shi, A prediction approach of fiber laser surface treatment using ensemble of metamodels considering energy consumption and processing quality, Green Manuf Open 2023 13 (1) (2022) N/A-N/A, https://doi.org/10.20517/gmo.2022.04.